Research Article Vol. 33, No. 3 / March 2016 / *Journal of the Optical Society of America A* 391

Journal of the Optical Society of America A
OPTICS, IMAGE SCIENCE, AND VISION

Near- and far-field scattering resonance frequency shift in dielectric and perfect electric conducting cylinders

ALEX J. YUFFA,[1,*] YAEL GUTIERREZ,[2] JUAN M. SANZ,[2] RODRIGO ALCARAZ DE LA OSA,[2] JOSÉ M. SAIZ,[2] FRANCISCO GONZÁLEZ,[2] FERNANDO MORENO,[2] AND GORDEN VIDEEN[1,2]

[1]*Army Research Laboratory, 2800 Powder Mill Road, Adelphi, Maryland 20783, USA*
[2]*Grupo de Óptica, Departamento de Física Aplicada, Universidad de Cantabria, Facultad de Ciencias, Avda. Los Castros s/n, 39005 Santander, Spain*
**Corresponding author: ayuffa@gmail.com*

Received 9 December 2015; revised 13 January 2016; accepted 13 January 2016; posted 20 January 2016 (Doc. ID 255504); published 23 February 2016

The ability to infer near-field scattering properties from far-field measurements is of paramount importance in nano-optics. Recently we derived an approximate formula for predicting the frequency shift between near- and far-field intensity peaks in the case of a dielectric sphere. In this work we demonstrate that almost an identical formula can be used to predict the resonance shift of a dielectric cylinder and a perfectly conducting cylinder. We find the redshift of the resonance peak of the perfect electric conducting cylinder to be approximately 2 orders of magnitude greater than for the dielectric cylinder. The errors in our approximate analytic formula for predicting the redshift are approximately only twice as great. Furthermore, we apply the redshift formula to a silicon cylinder and discuss its magneto-dielectric properties, which may be of interest in design of metamaterials.

OCIS codes: (220.4241) Nanostructure fabrication; (310.6628) Subwavelength structures, nanostructures; (260.5740) Resonance; (290.5870) Scattering, Rayleigh.

http://dx.doi.org/10.1364/JOSAA.33.000391

1. INTRODUCTION

We recently have derived an approximate, analytic formula for computing the frequency shift between the near- and far-field electric intensity peaks. This formula originally was derived for a dielectric scattering sphere [1]. In this paper, we demonstrate that a very similar formula holds true when a plane wave is scattered by a dielectric cylinder and a perfect electric conducting (PEC) cylinder; see Fig. 1. This frequency shift formula, termed the redshift formula, allows one to predict the near-field intensity resonances from the far-field measurements. One important application of the redshift formula is in designing and tuning nanoparticle resonances to be used as sources or detectors [2–4]. Generally speaking, it is more difficult to measure the near-field intensity than the far-field intensity, and, therefore, the redshift formula allows for an easy indirect near-field measurement.

Qualitatively, the redshift between the near- and far-field intensity can be explained by the damped harmonic oscillator model (see [1,5–7]). Furthermore, Moreno *et al.* [8] quantitatively demonstrate the evanescent wave contribution to the redshift, providing the mechanism for the shift. These early works become especially important when we consider the behavior of the redshift as a function of radial distance.

Throughout the paper, we assume that all fields are harmonic in time with a $\exp(-i\omega t)$ time factor, and all media are nonmagnetic. Unless explicitly noted otherwise, we use the Gaussian unit system and the notation defined in Table 1.

2. DIELECTRIC CYLINDER

If a unit plane wave, $\mathbf{E}^{\text{inc}} = \exp(ik_1 r \cos\theta)\hat{\mathbf{z}}$, is incident on an infinite cylinder centered at the origin of the coordinate system with its axis running parallel to $\hat{\mathbf{z}}$, then the scattered partial-wave electric field is given by ([9,10]; [11], Section 14.3)

$$\mathbf{E}_n^{\text{e}}(r,\theta) = g_n i^n A_n H_n(k_1 r)\cos(n\theta)\hat{\mathbf{z}}, \qquad n = 0, 1, \ldots, \tag{1a}$$

where

$$A_n = -\frac{a_n}{a_n + ic_n}, \tag{1b}$$

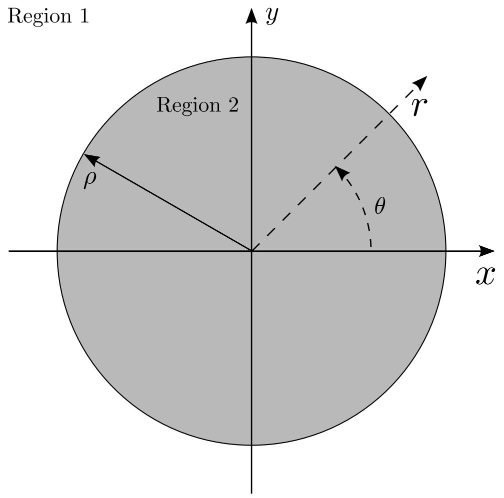

Fig. 1. Cross-sectional view of the cylinder of radius ρ is shown. The wave is incident from Region 1 and is scattered by the cylinder (Region 2).

$$a_n = J_n'(k_1\rho)J_n(k_2\rho) - \frac{k_2}{k_1}J_n(k_1\rho)J_n'(k_2\rho), \tag{1c}$$

$$c_n = Y_n'(k_1\rho)J_n(k_2\rho) - \frac{k_2}{k_1}Y_n(k_1\rho)J_n'(k_2\rho), \tag{1d}$$

and the prime denotes differentiation with respect to the argument. The superscript e on the left-hand side of Eq. (1a) reminds the reader of the electric polarization (TM mode), and the symbols $\{J_n, Y_n, H_n, g_n, r, \theta, k_1, k_2, \rho\}$ are defined in Table 1.

Let us define the angularly integrated scattered intensity as

$$\tilde{I}_n(\omega, r) = \int_{-\pi}^{\pi} \mathbf{E}_n(r,\theta)\cdot\mathbf{E}_n^*(r,\theta)\mathrm{d}\theta, \qquad r \geq \rho, \tag{2a}$$

where $*$ denotes the complex conjugate, and normalize it by $4/(k_1 r)$, i.e.,

$$I_n(\omega, r) = \frac{k_1 r}{4}\tilde{I}_n(\omega, r), \qquad r \geq \rho. \tag{2b}$$

As we will demonstrate, it is better to work with $I_n(\omega, r)$ instead of $\tilde{I}_n(\omega, r)$. In the far-field limit $k_1 r \gg 1$, the quantity $\tilde{I}_n(\omega, r)$ can be interpreted as the total scattered power because $\mathbf{E}_n(r,\theta)$ contains only the outgoing waves ([12], Section 5.2). Also in this limit, the electric field scales as $1/\sqrt{k_1 r}$ and thus, from Eq. (2b) we have that $I_n(\omega, r)$ is independent of the radial distance. In other words, $I_n(\omega, r)$ is constant on a circle of radius r if $k_1 r \gg 1$. However, from an application point of view, the quantity of interest in the near field is $\mathbf{E}_n\cdot\mathbf{E}_n^*$ or Eq. (2a). Clearly, these quantities are zero in the far field, and, therefore, they are not an ideal choice. On the other hand, in the near field we can think of Eq. (2b) as a measure of the scattered intensity on a circle of radius r. Of course, this interpretation is not identical to its far-field interpretation, but at least this quantity is nontrivial and has physical meaning in both the near- and far-field scattering regimes. Obviously, the physical reason for the difference in the interpretation comes from the distortion of the electric field near $r = \rho$, and this distortion is mandated by the boundary conditions on the surface of the scatterer. Last, we note that the rest of the prefactor in Eq. (2b) is simply chosen so that $I_n(\omega, r)$ has an elegant form in the far field. Our rationale for choosing to work with Eq. (2b) instead of Eq. (2a) is essentially the same as the argument presented in [13].

Table 1. Brief Description of the Symbols Used Throughout the Paper

Symbol	Description
J_n	Integer order Bessel function of the 1st kind
Y_n	Integer order Bessel function of the 2nd kind
H_n	Integer order Hankel function of the 1st kind
g_n	Neumann factor, i.e., $g_0 = 1$ and $g_n = 2$ for $n \geq 1$
(r, θ)	Polar coordinates, where $-\pi \leq \theta < \pi$
ω	Angular frequency
c	Speed of light in vacuum
ε_1	Permittivity of the host space (Region 1)
ε_2	Permittivity of the cylinder (Region 2)
$k_i = \sqrt{\varepsilon_i}\frac{\omega}{c}$	Wavenumber in the ith region
ρ	Radius of the cylinder

Returning to the scattering of the TM-polarized wave by the cylinder, we substitute Eq. (1) into Eq. (2b) to obtain

$$I_n^{\mathrm{e}}(\omega, r) = |A_n(\omega)|^2 f_n^{\mathrm{e}}(\omega, r), \qquad r \geq \rho, \tag{3a}$$

where

$$f_n^{\mathrm{e}} = \frac{\pi}{2}g_n k_1 r|H_n(k_1 r)|^2 \quad \text{and} \quad |A_n|^2 = \frac{a_n^2}{a_n^2 + c_n^2}. \tag{3b}$$

From the asymptotic form of the Hankel function, we see that Eq. (3) reduces to

$$I_n^{\mathrm{e}}(\omega) = g_n|A_n(\omega)|^2 \tag{4}$$

in the far-field limit, $k_1 r \gg 1$. The angular frequencies where Eq. (4) has local maxima can be found by solving the transcendental equation $c_n(\omega^{\mathrm{e}}) = 0$ for ω^{e} [1]. Let us denote their near-field counterparts by $\tilde{\omega}^{\mathrm{e}}$, i.e., Eq. (3a) has local maxima when $\omega = \tilde{\omega}^{\mathrm{e}}$. Both Eq. (3) and Eq. (4) conform to the requirements of the redshift formula derived in Appendix A of [1], which we summarize below.

Theorem 1 *If a function of the form*

$$I(\omega, r) = \frac{\mathbb{A}^2(\omega)}{\mathbb{A}^2(\omega) + \mathbb{B}^2(\omega)}f(\omega, r), \qquad \text{where} \left|\frac{\mathbb{A}(\omega_0)}{\dot{\mathbb{B}}(\omega_0)}\right| \leq 1,$$

has a local maximum in the far field when $\omega = \omega_0$, *and* $\mathbb{B}(\omega_0) = 0$, *then* $I(\omega, r)$ *has a near-field maximum that is shifted with respect to the far-field maximum by*

$$\Delta\omega(r) \approx \frac{1}{2}\left[\frac{\mathbb{A}(\omega_0)}{\dot{\mathbb{B}}(\omega_0)}\right]^2 \frac{\dot{f}(\omega_0, r)}{f(\omega_0, r)}.$$

Thus, from Theorem 1, we immediately obtain

$$\Delta\omega^{\mathrm{e}}(r) = \tilde{\omega}^{\mathrm{e}}(r) - \omega^{\mathrm{e}} \approx \frac{1}{2}\left[\frac{a_n(\omega^{\mathrm{e}})}{\dot{c}_n(\omega^{\mathrm{e}})}\right]^2 \frac{\dot{f}_n^{\mathrm{e}}(\omega^{\mathrm{e}}, r)}{f_n^{\mathrm{e}}(\omega^{\mathrm{e}}, r)}, \tag{5}$$

where the overdot $\cdot$ denotes differentiation with respect to ω. The above redshift formula allows one to compute the frequency shift dependence on the radial distance r. It is interesting to note that, in the Rayleigh limit, the ratio $a_n/\dot{c}_n$ in Eq. (5) reduces to a particular simple form, namely,

$$\frac{a_0}{\dot{c}_0} = \frac{\pi\omega}{4}(x_1^2 - x_2^2) \quad \text{and} \quad \frac{a_1}{\dot{c}_1} = \frac{\pi\omega}{32}(x_1^2 - x_2^2)x_1^2, \tag{6}$$

where $x_i = k_i\rho$. To derive Eq. (6), we substitute the first three terms in the power series representation of J_n and Y_n ([14], Section 10.2, Section 10.8) into $a_n/\dot{c}_n$ and retain only the leading term in ρ.

Analogous results can be derived for a magnetically polarized incident wave (TE mode). If we take the incident wave to be $\mathbf{H}^{\mathrm{inc}} = \sqrt{\epsilon_1}\exp(ik_1 r\cos\theta)\hat{\mathbf{z}}$ so that $\mathbf{E}^{\mathrm{inc}}\cdot(\mathbf{E}^{\mathrm{inc}})^* = 1$, then the scattered partial-wave electric field is given by ([11], Section 14.3)

$$\mathbf{E}_n^{\mathrm{m}}(r,\theta) = -g_n \mathrm{i}^{n+1} B_n\left[\frac{n}{k_1 r} H_n(k_1 r)\sin(n\theta)\hat{\mathbf{r}} + H_n'(k_1 r)\cos(n\theta)\hat{\boldsymbol{\theta}}\right], \tag{7a}$$

where

$$B_n = -\frac{b_n}{b_n + \mathrm{i}d_n}, \tag{7b}$$

$$b_n = \frac{k_2}{k_1} J_n'(k_1\rho)J_n(k_2\rho) - J_n(k_1\rho)J_n'(k_2\rho), \tag{7c}$$

$$d_n = \frac{k_2}{k_1} Y_n'(k_1\rho)J_n(k_2\rho) - Y_n(k_1\rho)J_n'(k_2\rho), \tag{7d}$$

and the superscript m on the left-hand side of Eq. (7a) reminds the reader of the magnetic polarization (TE mode). Substituting Eq. (7) into Eq. (2) yields

$$I_n^{\mathrm{m}}(\omega, r) = |B_n(\omega)|^2 f_n^{\mathrm{m}}(\omega, r), \qquad r \geq \rho, \tag{8a}$$

where

$$f_n^{\mathrm{m}} = \frac{\pi}{2} g_n\left[\frac{n^2}{k_1 r}|H_n(k_1 r)|^2 + k_1 r|H_n'(k_1 r)|^2\right], \tag{8b}$$

and

$$|B_n|^2 = \frac{b_n^2}{b_n^2 + d_n^2}. \tag{8c}$$

The far-field form of Eq. (8), namely,

$$I_n^{\mathrm{m}}(\omega) = g_n|B_n(\omega)|^2, \qquad k_1 r \gg 1, \tag{9}$$

follows immediately from the asymptotic form of the Hankel function, and the local maxima of Eq. (9) are given by the solution to the transcendental equation $d_n(\omega^{\mathrm{m}}) = 0$. As in the TM case, we use Theorem 1 to obtain the redshift formula

$$\Delta\omega^{\mathrm{m}}(r) = \tilde{\omega}^{\mathrm{m}}(r) - \omega^{\mathrm{m}} \approx \frac{1}{2}\left[\frac{b_n(\omega^{\mathrm{m}})}{\dot{d}_n(\omega^{\mathrm{m}})}\right]^2 \frac{\dot{f}_n^{\mathrm{m}}(\omega^{\mathrm{m}}, r)}{f_n^{\mathrm{m}}(\omega^{\mathrm{m}}, r)}. \tag{10}$$

Again, we see that in the Rayleigh limit the terms relating to the scattering coefficients reduce to a simple form

$$\frac{b_0}{\dot{d}_0} = \frac{\pi\omega}{32}(x_1^2 - x_2^2)x_1^2 \quad \text{and} \quad \frac{b_1}{\dot{d}_1} = \frac{\pi\omega}{4}\left(\frac{x_1^2 - x_2^2}{x_1^2 + x_2^2}\right)x_1^2. \tag{11}$$

To demonstrate the accuracy of the approximate redshift formulas [Eqs. (5) and (10)], we have computed the relative error as a function of the scaled distance r/ρ for several resonances. For convenience, we identify these resonances in Fig. 2 via the unitless parameter $x^{\mathrm{e,m}} = \sqrt{\epsilon_1}\frac{\omega^{\mathrm{e,m}}}{c}\rho$. Figure 2 shows that the relative error is less than 5% and the error approaches zero in the far field as expected. To demonstrate that the near-field peaks are indeed redshifted with respect to their far-field counterparts, we plot the scaled redshift as a function of the scaled distance; see Fig. 3 and note the negative sign on the vertical axis. Furthermore, observe that the redshift is maximum near the surface of the particle, i.e., $r/\rho = 1$. Of course, this is an expected behavior because the redshift is essentially caused by the evanescent waves [1,8]. We also note that the redshift is identical for the $n = 0$ TE mode and the $n = 1$ TM mode because, from Eq. (8a) and Eq. (3a), we have $2I_{n=0}^{\mathrm{m}} = I_{n=1}^{\mathrm{e}}$. This relationship also explains why $b_0/\dot{d}_0 = a_1/\dot{c}_1$ in the Rayleigh limit; see Eq. (11) and Eq. (6).

Having established the validity of the redshift formula, we illustrate the applicability with example dielectric metamaterials in which high-refractive-index cylinders are used. In particular, we consider a silicon cylinder in the near-infrared region where

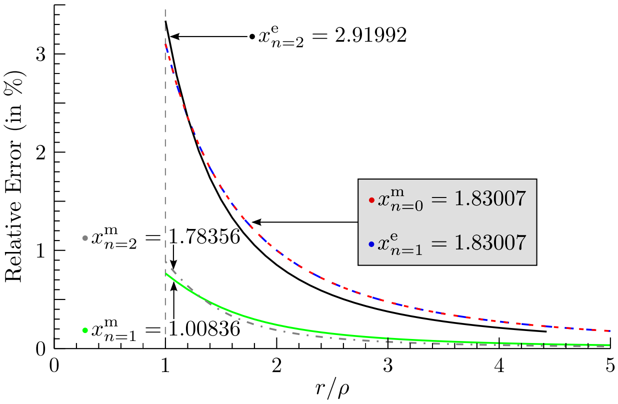

Fig. 2. In the dielectric ($\varepsilon_2 = 100$) cylinder case, the relative error associated with the redshift formula in Eq. (5) is shown as a function of the scaled radial distance.

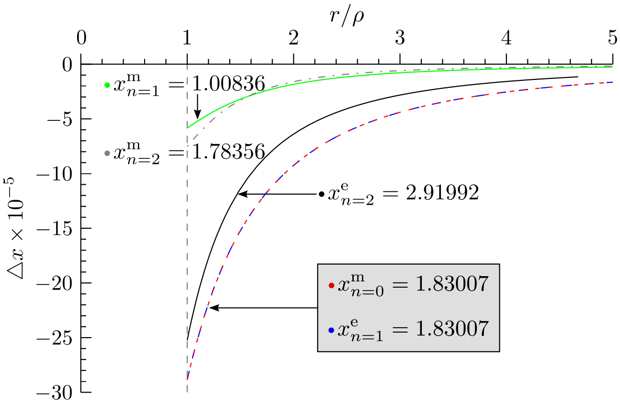

Fig. 3. In the dielectric ($\varepsilon_2 = 100$) cylinder case, the scaled redshift $\Delta x^{\mathrm{e,m}}$ is shown as a function of the scaled radial distance.

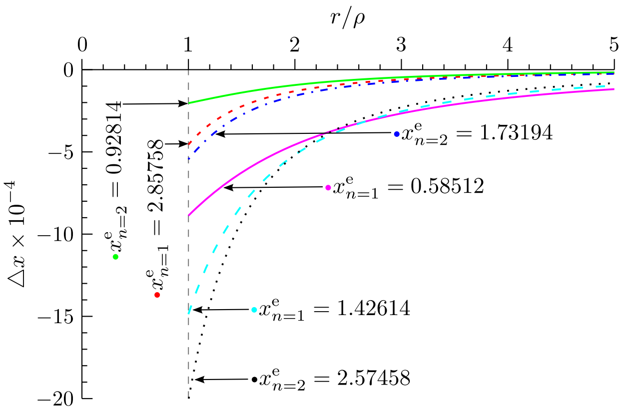

Fig. 4. Scaled redshift Δx^{e} is shown as a function of the scaled radial distance from a silicon ($\varepsilon_2 = 16$) cylinder.

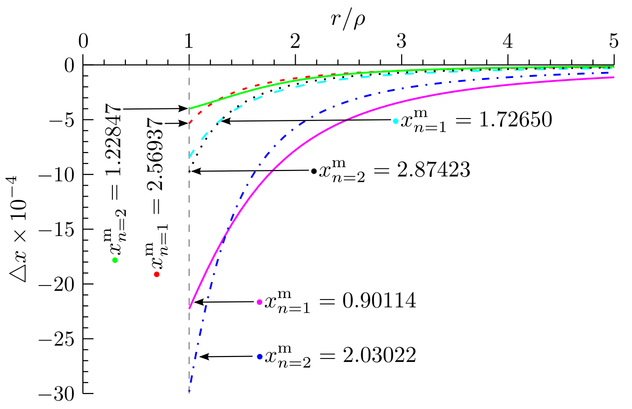

Fig. 5. Scaled redshift Δx^{m} is shown as a function of the scaled radial distance from a silicon ($\varepsilon_2 = 16$) cylinder. The curves $x^{\mathrm{m}}_{n=1} = 0.90114$ and $x^{\mathrm{m}}_{n=2} = 2.03022$ show magnetic modes for which the redshift is stronger in the magnetic mode than in the electric mode.

the permittivity can be as high as 16. From an application point of view, such metamaterials are of great interest because they may offer complete control of light at wavelength scales [15–17]. The redshift as a function of the scaled radial distance is shown for TM and TE polarization states in Fig. 4 and Fig. 5, respectively. By comparing these figures, we see that there are two magnetic resonances (see curves labeled $x^{\mathrm{m}}_{n=1} = 0.90114$ and $x^{\mathrm{m}}_{n=2} = 2.03022$ in Fig. 5) for which the redshift of the magnetic mode is stronger than that of the electric mode. The stronger response in the magnetic mode in silicon particles is possible because of the relatively high index of refraction [18–20]. We note that these magneto-dielectric properties are becoming increasingly important in the design of metamaterials. Therefore, our simple example may be of value to optical engineers.

3. PERFECT CONDUCTING CYLINDER

If we repeat the derivation presented in Section 2 for a PEC cylinder, then the a_n and c_n coefficients in Eq. (1) become ([11], Section 14.2)

$$a_n = J_n(k_1\rho) \quad \text{and} \quad c_n = Y_n(k_1\rho), \tag{12a}$$

and the b_n and d_n coefficients in Eq. (7) become

$$b_n = J'_n(k_1\rho) \quad \text{and} \quad d_n = Y'_n(k_1\rho). \tag{12b}$$

Although the rest of the equations in Section 2 remain unchanged (except, of course, for the Rayleigh limit formulas), the interpretation changes. In the PEC cylinder, the fields inside the cylinder vanish and the scattered field originates from the surface currents.

By comparing Fig. 2 with Fig. 6, we see that the relative error in the PEC case is about twice the error of the dielectric case. This is a very modest decrease in accuracy if we consider the 2 orders of magnitude increase in the redshift; see Figs. 3 and 7. The main mechanism that produces the redshift in perfect dielectrics is the leakage of the evanescent waves from the internal resonance modes [1]. Moreover, we expect the redshift in the dielectric case to be small relative to its metallic counterpart [8].

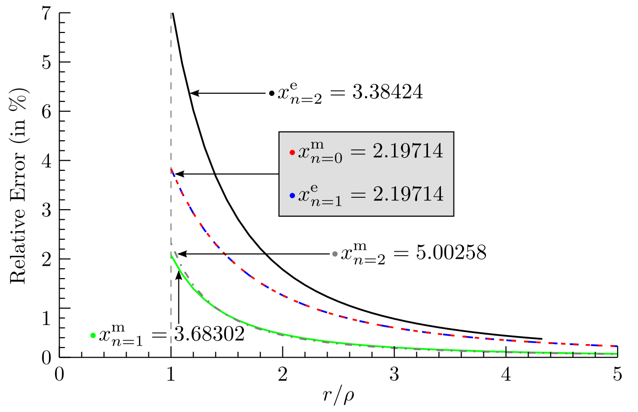

Fig. 6. In the PEC cylinder case, the relative error associated with the redshift formula in Eq. (10) is shown as a function of the scaled radial distance.

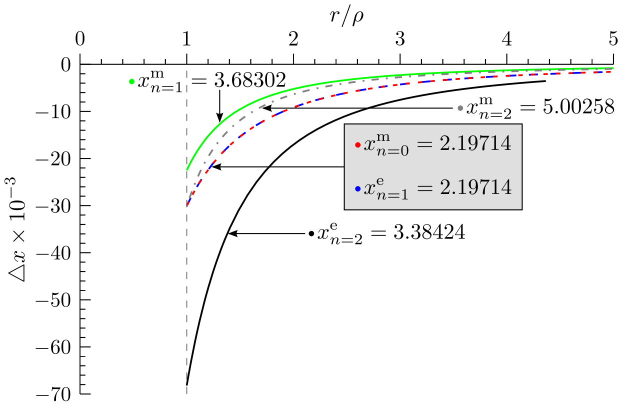

Fig. 7. In the PEC cylinder case, the scaled redshift $\Delta x^{\mathrm{e,m}}$ is shown as a function of the scaled radial distance.

4. CONCLUSIONS

We have demonstrated that the previously derived redshift formula is also applicable for both dielectric and PEC scattering cylinders. This formula predicts the frequency shift between the near-field electric intensity peaks and their far-field counterparts, which are assumed to be known. Furthermore, we speculate the redshift formula also should be applicable in many other scattering situations where the absolute value squared of the partial scattering amplitudes can be expressed in the same form. To convince the reader of this, we apply the formula to another canonical shape and consider two extreme scattering regimes, namely, scattering by a perfect dielectric and a perfect conductor. Finally, the results presented in this manuscript along with the results of [1] suggest that the redshift formula is of wider applicability than previously thought.

REFERENCES

1. A. J. Yuffa, Y. Gutierrez, J. M. Sanz, R. Alcaraz de la Osa, J. M. Saiz, F. González, F. Moreno, and G. Videen, “Frequency shift between near- and far-field scattering resonances in dielectric particles,” J. Opt. Soc. Am. A **32**, 1638–1642 (2015).
2. N. G. Khlebtsov and L. A. Dykman, “Optical properties and biomedical applications of plasmonic nanoparticles,” J. Quant. Spectrosc. Radiat. Transfer **111**, 1–35 (2010).
3. S. Schlücker, “Surface-enhanced Raman spectroscopy: concepts and chemical applications,” Angew. Chem. Int. Ed. **53**, 4756–4795 (2014).
4. A. N. Grigorenko, N. W. Roberts, M. R. Dickinson, and Y. Zhang, “Nanometric optical tweezers based on nanostructured substrates,” Nat. Photonics **2**, 365–370 (2008).
5. J. Chen, P. Albella, Z. Pirzadeh, P. Alonso-González, F. Huth, S. Bonetti, V. Bonanni, J. Åkerman, J. Nogués, P. Vavassori, A. Dmitriev, J. Aizpurua, and R. Hillenbrand, “Plasmonic nickel nanoantennas,” Small **7**, 2341–2347 (2011).
6. M. A. Kats, N. Yu, P. Genevet, Z. Gaburro, and F. Capasso, “Effect of radiation damping on the spectral response of plasmonic components,” Opt. Express **19**, 21748–21753 (2011).
7. J. Zuloaga and P. Nordlander, “On the energy shift between near-field and far-field peak intensities in localized plasmon systems,” Nano Lett. **11**, 1280–1283 (2011).
8. F. Moreno, P. Albella, and M. Nieto-Vesperinas, “Analysis of the spectral behavior of localized plasmon resonances in the near- and far-field regimes,” Langmuir **29**, 6715–6721 (2013).
9. A. J. Yuffa and J. A. Scales, “Measuring the void: theoretical study of scattering by a cylindrical annulus,” J. Quant. Spectrosc. Radiat. Transfer **131**, 188–193 (2013).
10. A. J. Yuffa, P. A. Martin, and J. A. Scales, “Scattering from a large cylinder with an eccentrically embedded core: an orders-of-scattering approximation,” J. Quant. Spectrosc. Radiat. Transfer **133**, 520–525 (2014).
11. J. G. Van Bladel, *Electromagnetic Fields*, 2nd ed., IEEE Press Series on Electromagnetic Wave Theory (Wiley-IEEE, 2007),
12. M. I. Mishchenko, *Electromagnetic Scattering by Particles and Particle Groups: An Introduction* (Cambridge University, 2014).
13. B. Messinger, K. von Raben, R. Chang, and P. Barber, “Local fields at the surface of noble-metal microspheres,” Phys. Rev. B **24**, 649–657 (1981).
14. F. W. J. Olver, D. W. Lozier, R. F. Boisvert, and C. W. Clark, eds., *NIST Handbook of Mathematical Functions* (Cambridge University, 2010).
15. P. Spinelli, M. Verschuuren, and A. Polman, “Broadband omnidirectional antireflection coating based on subwavelength surface Mie resonators,” Nat. Commun. **3**, 692 (2012).
16. A. Arbabi, Y. Horie, M. Bagheri, and A. Faraon, “Dielectric metasurfaces for complete control of phase and polarization with subwavelength spatial resolution and high transmission,” Nat. Nanotechnol. **10**, 937–943 (2015).
17. Y. Li, S. Kita, P. Muñoz, O. Reshef, D. I. Vulis, M. Yin, M. Lončar, and E. Mazur, “On-chip zero-index metamaterials,” Nat. Photonics **9**, 738–742 (2015).
18. A. B. Evlyukhin, C. Reinhardt, A. Seidel, B. S. Luk’yanchuk, and B. N. Chichkov, “Optical response features of Si-nanoparticle arrays,” Phys. Rev. B **82**, 045404 (2010).
19. A. B. Evlyukhin, C. Reinhardt, and B. N. Chichkov, “Multipole light scattering by nonspherical nanoparticles in the discrete dipole approximation,” Phys. Rev. B **84**, 235429 (2011).
20. A. García-Etxarri, R. Gómez-Medina, L. S. Froufe-Pérez, C. López, L. Chantada, F. Scheffold, J. Aizpurua, M. Nieto-Vesperinas, and J. J. Sáenz, “Strong magnetic response of submicron silicon particles in the infrared,” Opt. Express **19**, 4815–4826 (2011).